RESEARCH ARTICLE

Brain Tumor Classification Using Hybrid Single Image Super-Resolution Technique With ResNext101_32 × 8d and VGG19 Pre-Trained Models

SAEED MOHSEN[1,2], **ANAS M. ALI**[3,4], **EL-SAYED M. EL-RABAIE**[4], **AHMED ELKASEER**[5,6], **STEFFEN G. SCHOLZ**[5,7], **AND ASHRAF MOHAMED ALI HASSAN**[8]

[1]Department of Electronics and Communications Engineering, Al-Madinah Higher Institute for Engineering and Technology, Giza 12947, Egypt
[2]Department of Artificial Intelligence Engineering, Faculty of Computer Science and Engineering, King Salman International University (KSIU), El Tor, South Sinai 46511, Egypt
[3]Robotics and Internet of Things, Prince Sultan University, Riyadh 12435, Saudi Arabia
[4]Department of Electronics and Electrical Communications Engineering, Faculty of Electronic Engineering, Menoufia University, Menouf 32952, Egypt
[5]Institute for Automation and Applied Informatics, Karlsruhe Institute of Technology, 76344 Karlsruhe, Germany
[6]Department of Production Engineering and Mechanical Design, Faculty of Engineering, Port Said University, Port Fuad 42526, Egypt
[7]College of Engineering, Future Manufacturing Research Institute, Swansea University, SA1 8EN Swansea, U.K.
[8]Department of Electronics and Communications Engineering, October High Institute for Engineering and Technology, 6th of October City 12596, Egypt

Corresponding author: Ahmed Elkaseer (ahmed.elkaseer@kit.edu)

ABSTRACT High-quality images acquired from medical devices can be utilized to aid diagnosis and detection of various diseases. However, such images can be very expensive to acquire and difficult to store, and the process of diagnosis can consume significant time. Automatic diagnosis based on artificial intelligence (AI) techniques can contribute significantly to overcoming the cost and time issues. Pre-trained deep learning models can present an effective solution to medical image classification. In this paper, we propose two such models, ResNext101_32×8d and VGG19 to classify two types of brain tumor: pituitary and glioma The proposed models are applied to a dataset consisting of 1,800 MRI images comprising in two classes of diagnoses; glioma tumor and pituitary tumor. A single-image super-resolution (SISR) technique is applied to the MRI images to classify and enhance their basic features, enabling the proposed models to enhance particular aspects of the MRI images and assist the training process of the models. These models are implemented using PyTorch and TensorFlow frameworks with hyper-parameter tuning, and data augmentation. Experimentally, receiver operating characteristic curve (ROCC), the error matrix, Precision, and Recall are used to analyze the performance of the proposed model. Results obtained demonstrate that VGG19 and ResNext101_32 × 8d achieved testing accuracies of 99.98% and 100%, and loss rates of 0.0120 and 0.108, respectively. The F1-score, Precision, Recall, and the area under the ROC for VGG19 were 99.89%, 99.90%, 99.89%, and 100%, respectively, while for the ResNext101_32 × 8d they were all 100%. The proposed models when applied to MRI images to provide a quick and accurate approach to distinguishing between patients with pituitary and glioma tumors, and could aid doctors and radiologists in the screening of patients with brain tumors.

INDEX TERMS Single image super-resolution, visual geometry group (VGG)-19, ResNext101_32 × 8d, brain tumor classification, magnetic resonance imaging (MRI), medical image analysis.

The associate editor coordinating the review of this manuscript and approving it for publication was Jiankang Zhang.

I. INTRODUCTION

An important issue in medicine is classification of brain tumors [1], [2] to decide on treatment type. This is a

challenging issue because tumor cells are heterogeneous by nature. Doctors, of course, are important in the diagnosis of this disease, but would benefit from a helpful tool to aid rapid diagnosis [3]. Today, diagnostic systems based on computer-aided technology provide an effective means for diagnosing brain tumors via magnetic resonance imaging (MRI) [4]. MRI is the most common technique used for classifying brain tumors, because of its high image quality [5]. Artificial intelligence (AI) is also being considered as a key enabler to assist in resolving issues around brain tumor classification. In particular, the development of high-performance deep learning models (DLMs) with high levels of accuracy would be a significant step towards a fast, high-precision method for detection and diagnosis of brain tumors in patients.

Machine learning and deep learning models are being utilized to classify and diagnose brain tumors [6], but, the low accuracy of existing models is a challenge that needs to be addressed [7]. Deep convolutional neural networks (CNNs) are playing an effective role in detecting the presence of brain tumors and diagnosing tumor type via medical imaging using MRI, which has been used to successfully detect patients infected with brain tumors. However, a disadvantage of these networks is the long time required to train the models [8]. Low accuracy can be significantly improved by using pre-trained DLMs, such as VGG [9], DenseNet [10], ResNet [11], GoogLeNet [12], AlexNet [13], MobileNet [14], and EfficientNet [15] which can also reduce training time. Speech recognition [16] language modeling [17], human activity recognition [18], and image processing [19] are already making good use of such models. Pre-trained models are more convenient since they require less training time. However, achieving a sufficiently high accuracy in classifying brain tumors remains a significant challenge.

This paper reports on implementing ResNext101_32 $\times$ 8d and VGG19 models to enhance the accuracy of detection and classification of brain tumor using hyper-parameter optimization. These two models are based on a transfer learning process, and have the advantage of architectural simplicity, which can reduce computational cost (training time). The models were tested and trained on a dataset available in the Kaggle repository. In addition, a data augmentation technique was employed on the dataset used in order to overcome its deficiency of the available medical images.

The primary contributions of this paper are:
- Implementation of robust ResNext101_32 $\times$ 8d and VGG19 to distinguish between glioma and pituitary brain images/cases for fast and more accurate diagnoses;
- Using ResNext101_32 $\times$ 8d and VGG19 with hyper-parameter optimization to successfully achieve substantially greater test accuracy for a graphics processing unit (GPU);
- Applying a single image super-resolution (SISR) technique for the two models based on a generative

adversarial network (GAN) algorithm to improve the resolution of the MRI images;
- Evaluating the performance of the models with alternative evaluation measures based on an assessment of the quality of images in a dataset of 1,800 MRI images of the brain;
- Improving VGG19 accuracy by using k-fold cross-validation;
- Comparing the results achieved by the proposed models for the MRI image classification with different state-of-the-art models.

The remainder of this paper is as follows: Section II presents a brief review of similar work. Section III introduces the theoretical background to transfer learning. Section IV presents the proposed DLMs, dataset description, and performance metrics utilized. Section V presents the experimental results. The results are discussed in Section VI. Section VII offers conclusions and suggestions for further work.

II. RELATED WORK
The literature contains reports of a number of DL models for classifying brain tumors using MRI images of the brain [20], [21], [22], [23], but a satisfactory level of accuracy has not always been achieved. In [20], Afshar, et al., introduced a capsule neural network method to classify brain tumor diseases. This model was applied on a 3,064-image dataset and had an 86.56% accuracy. In [21], the same authors proposed a CNN model enhanced by a genetic algorithm (GA) to recognize brain tumors and applied the model to a dataset of 600 different images, with the best accuracy achieved is 94.2%. Saxena et al., [22] applied three models, ResNet-50, Inception-V3, and VGG-16, to a set of just over 250 images, divided into 183 for training, 50 for validation, and 20 for testing. The respective accuracies for Inception-V3, VGG-16 and ResNet-50 were 55%, 90%, and 95%. Zhou et al., [23] presented a combined DenseNet-Long ShortTermory model for identifying brain tumors and tested the model on a set of data comprising: 708 meningioma, 930 pituitary, and 1,426 glioma patients. The model achieved a 92.13% accuracy.

Researchers [24], [25], [26], [27], and [28] presented machine and deep learning architectures to detect brain tumors in patients. In [24], Cheng et al., introduced an SVM model and attained a 91.28% accuracy with a dataset of 1,426 glioma and 930 pituitary images. A model using CNN architecture was applied to a dataset of 3,064 MRI images [25] and attained 84.19% accuracy. Kaplan et al., [26] applied a k-nearest neighbor (KNN) model with nLBP feature extraction approach, and achieved 95.56% accuracy. Pashaei et al., [27] implemented a CNN model with an extreme learning machine (ELM) method and trained using 70% of a dataset that contained 3,064 brain tumor cases. The model was then used to assess the other 30% and attained an accuracy of 93.68%. In [28], Zacharaki et al., proposed SVM-KNN models for brain tumor classification, which

were applied to a dataset of 102 MRI images, achieving an overall accuracy of 85%.

Kurup et al., [29] utilized the architecture of a CapsNet model based on three classes to predict the presence of brain tumors. It applied capsule neural networks to a set of data comprising 3,170 images with an accuracy of 92.6%. In [30], Das et al., applied a CNN for brain tumor detection with a dataset containing three classes of 1,426 glioma, 708 meningioma, and 930 pituitary cases. The accuracy and precision achieved were 94.39% and 93.33%, respectively. Ullah et al., [31] proposed to classify brain tumors using MRI images via an artificial neural network (ANN), and attained a testing accuracy of 95.80%. In [32], Huang et al., used a CNN to classify brain tumors and attained an overall accuracy of 95.49%. In [33], Kalaiselvi et al., diagnosed brain tumors using a CNN with 96.00% accuracy. Li et al., [34] used a hidden Markov model (HMM) for real-time classification of brain tumors and achieved an accuracy of 96.88%. Noreen et al., [35] introduced two models: Xception and Inception-V3, and used 3,064 images to achieve accuracies of 93.79% and 94.34%, respectively.

Rehman et al. [36] classified microscopic brain tumors using a 3D CNN. This model was applied to the BraTS datasets, using the *k*-fold cross-validation method, achieving a 96.67% accuracy. In [37], Rehman et al., implemented GoogLeNet, VGGNet, and AlexNet models, utilized 3,064 images, and classified three types of tumors. Sharif et al., [38] presented an InceptionV3 model for brain tumor recognition, with an achieved 93.7% accuracy. In [39], Muzammil et al., proposed a multimodal image fusion algorithm for diagnoses using MRI images. It was applied with a convolutional sparse coding method which used the entropy theorem to assess the performance of the algorithm. Maqsood et al., [40] investigated brain tumor detection using U-NET CNN and fuzzy logic algorithms, but did not quote a success rate. Their literature review showed that despite significant research into detecting the presence of glioma or pituitary tumors in the brain via MRI images, improvements more accurate methods are still needed.

III. BACKGROUND FOR TRANSFER LEARNING

Transfer learning is a machine learning technique whereby a model trained for one purpose is subsequently used for another. The weights from the pre-trained model are applied as a starting point for training using a different dataset for a different issue. A significant advantage of transfer learning is a faster training/learning process. Another advantage is achieving higher performance with less data due to the weights obtained from the previous training being used. A higher performance can be achieved by the addition of a fully connected layer to the existing model.

Transfer learning is usually associated with relatively small datasets, such as biomedical images. If a DLM is trained *ab initio*, the training process requires a large amount of data and time. Thus, it is convenient to utilize a pre-trained model and fine-tune its performance to accelerate the training process. There are many successful pre-trained CNN models used in the classification of medical images, including ResNext101_32 × 8d and VGG19 [41], which were pre-trained using the ImageNet dataset, which consists of 1.3×10^6 RGB images of 224 × 224 pixels and with 1000 classes. It is proposed to use VGG19 and ResNext101_32 × 8d as pre-trained DLMs for transfer learning to classify brain tumor types.

IV. METHODOLOGY

ResNext101_32 × 8d and VGG19 models are employed here to classify two categories of brain tumors and were applied to a dataset consisting of 1,800 MRI brain images. These models were chosen due to their robust performance and to be convenient for processing spatial data [42].

A. THE PROPOSED SISR TECHNIQUE WITH RESNEXT101_32 × 8dI

In this work, before classification by the ResNext101_32×8d model, a SISR technique was applied to the chosen MRI brain tumor images. Fig. 1 illustrates the architecture of the SISR technique with ResNext101_32 × 8d model. The SISR is based on a GAN algorithm to produce high-resolution images. The SISR consists of two phases: the first is the generator, and the second is the discriminator. The generator comprises an input layer with a shape of 64 × 64 × 3 and a kernel size of 3, followed by an up-sampling block containing a convolutional layer and a Parametric Rectified Linear Unit (PReLU) layer, this is followed by a residual block which repeats every sixteen iterations and comprises: a convolutional layer, a Batch-normalization layer, a PReLU layer, another convolutional layer, another Batch-normalization layer, and an Add layer. These are followed by three layers: convolutional, Batch-normalization, and Add, followed by two blocks Convolutional, Lambda, and PReLU. Finally, the output layer is activated by a sigmoid activation function.

Every convolutional layer (conv-layer_has 3 × 3 kernels and 64 filters. The discriminator model comprises an input layer, a convolutional layer, and a ReLU layer, followed by seven repeated blocks containing a convolutional layer, a Batch-normalization layer, and a ReLU, this is followed by a block that includes a flatten layer, a dense layer, and ReLU, this block is repeated three times. Next, there is a dense layer and an output layer with a sigmoid activation function. The dimensions of the high-resolution (HR) images are 256 × 256 × 3 and the low-resolution (LR) images are generated from the high-resolution images. The LR images have dimensions of 64 × 64 × 3. So, the HR is divided by a factor of 4 in order to obtain the dimensions of the LR images. For the SISR technique, only 1700 images were used from the three thousand MRI images available due to the generator model used in the training process being slow. The images were normalized to the range from 1 to −1. 1,550,659 trainable parameters were available for the generator model-based SISR technique.
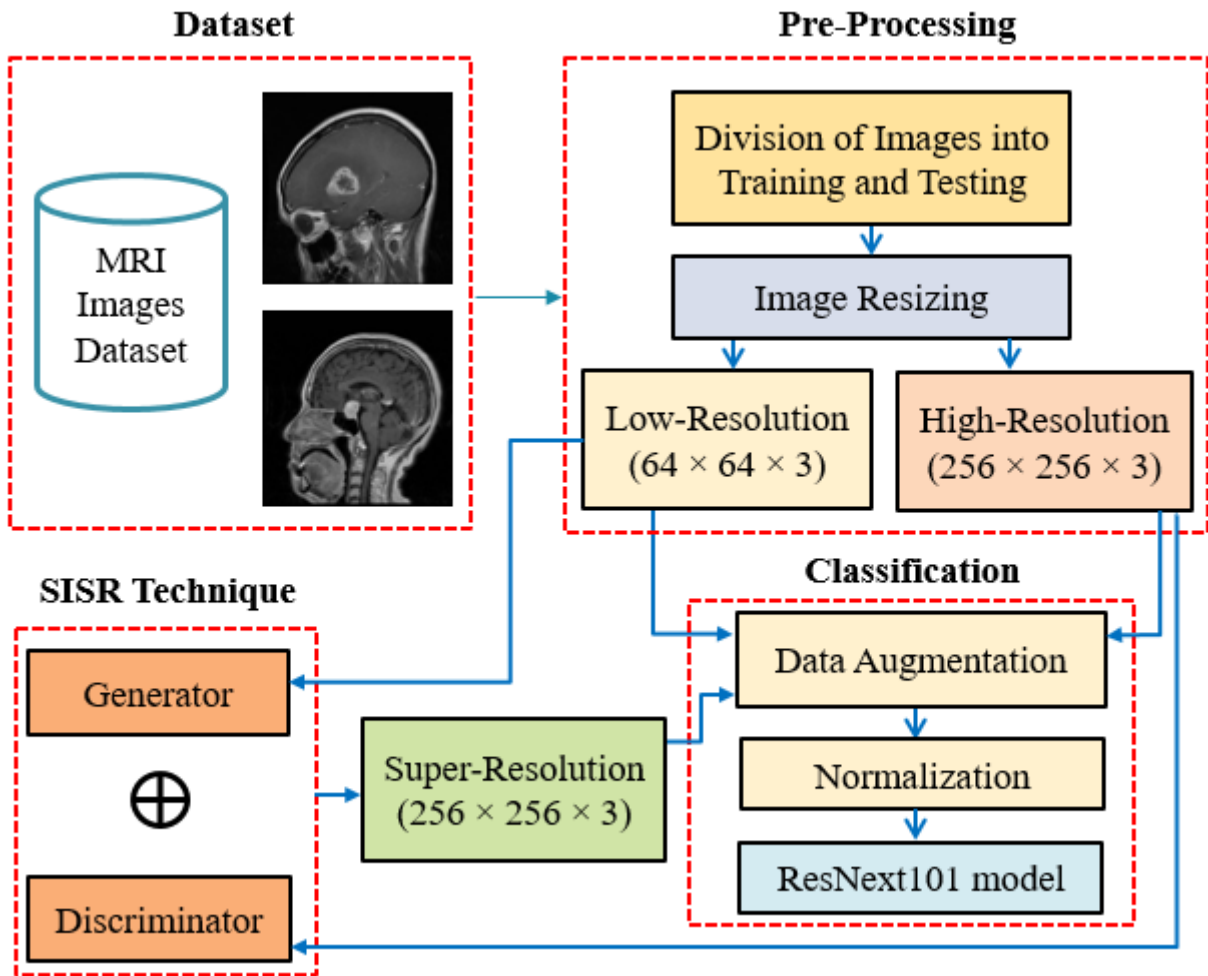
FIGURE 1. The workflow of the proposed SISR technique with ResNext101_32 × 8d model.

The ResNext101_32 × 8d model consists of 344 layers including: 104 batch normalization layers, 104 conv-layers, 100 ReLU layers, 33 bottleneck layers, a single max-pooling layer (MPL), a single adaptive average layer, and one linear layer. The input MRI images have equal width and height of 224 pixels. A binary cross-entropy loss function was used with the ResNext101_32 × 8d, to estimate the difference between predicted and true values, with the loss function calculated using Eq. (1), with y the true output label, and $\hat{y}$ the predicted label, and N represents the number of classes. An Adam algorithm was used as an optimizer. A batch size of 16 was used to train the ResNext101_32 × 8d model, with 10 training epochs, and a 0.0001 learning rate. The overall trainable parameters for the ResNext101_32 × 8d model were 86,746,434.

$$loss = -[y log\,(\hat{y}) + (1 - y)\,log\,(1 - \hat{y})] \qquad (1)$$

B. THE PROPOSED SISR TECHNIQUE WITH VISUAL GEOMETRY (VGG)-19

In this work, a SISR technique was also used on the MRI brain tumor images before classification by VGG19. Fig. 2

displays the architecture of the proposed VGG19 model, which comprises 19 layers: three fully connected layers and sixteen 2-D conv-layers, each of which is followed by a 2-D MPL. Training VGG19 takes less time than other pre-trained models while also having high classification accuracy.

As previously, the input MRI images have equal width and height of 224 pixels. First, a 2-D convolutional layer was applied separately to each input image, with a ReLU activation function to extract spatial features. This layer has 64 filters, a kernel with 3 × 3 matrix shape, followed by another convolutional layer with 64 filters with a ReLU function. To make the convolution output less complex an MPL with a 2 × 2 matrix, carried out a downsampling procedure.

Third, there were two conv-layers having 128 filters, a kernel with a 3 × 3 matrix, and utilizing a ReLU function. These added layers enable the VGG19 to discern higher-level features that might have been missed in the previous conv-layers. Fourth, an MPL with a 2 × 2 pool size is followed by four 2-D conv-layers having a configuration of 256 filters, a kernel with a 3 × 3 matrix, followed by an MPL and then four 2-D conv-layers having a configuration of 512 filters
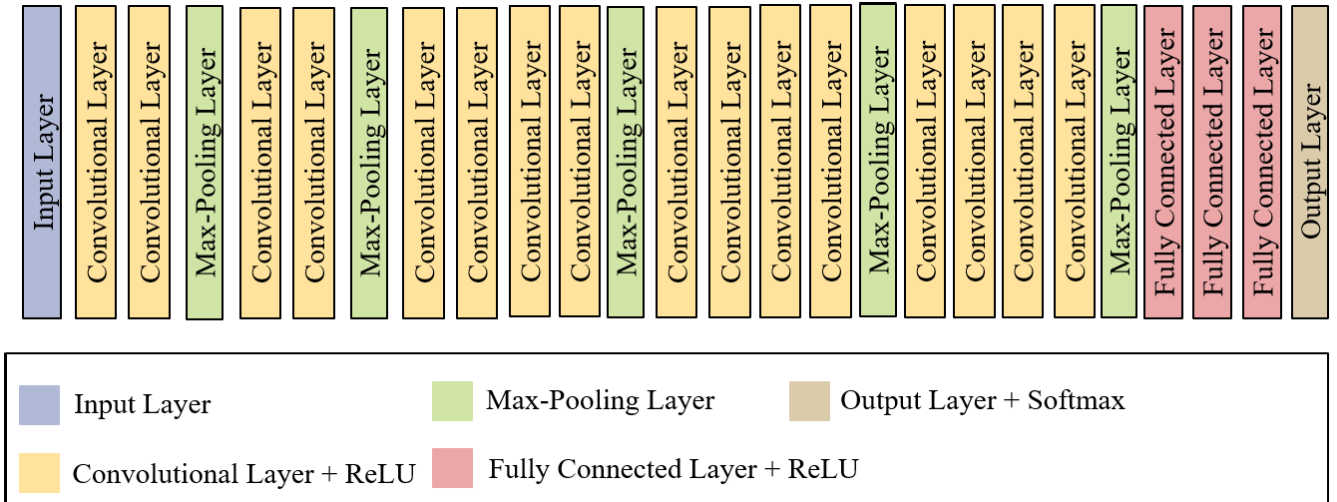
FIGURE 2. The proposed VGG19 model architecture.

with an MPL. Fifth, four more 2-D conv-layers having a configuration of 1024 filters, followed by an MPL. Sixth, two fully connected layers are configured with 4096 neurons and a ReLU activation function, followed by a fully connected layer with 1000 neurons. Finally, the output is reduced to just two classes by the application of a softmax activation function.

The difference between predicted and true values for the VGG19 was obtained using a binary cross-entropy loss function, with the loss function calculated using Eq. (1), with N the number of classes, y the true output label, and $\hat{y}$ the predicted label. Again an Adam algorithm was used as an optimizer [43]. It was found that a batch size of 30 with 50 training epochs were best to train the VGG19 model for classification of brain tumors. The total number of trainable parameters for this model was 2,325,568. Table 1 presents a summary of the layers for the VGG19 model.

Fig. 3 shows the workflow for the proposed VGG19 model. There are six steps, the first was uploading the MRI images dataset used, which were separated into images for testing and training. The second step was pre-processing the MRI images i.e., image normalization. The third step was to define the number of training epochs. The fourth was the training of the model using the designated MRI images via a fitting function. The fifth step was to test the prediction capacity of the VGG19 model using the MRI test images. The final step was to evaluate the performance of the model using different metrics on the MRI test images.

C. DATASET DESCRIPTION

Fig. 4 shows four of the MRI brain images from the dataset supplied by the Kaggle repository and used for classification [44]. There were 1,800 MRI brain images of two classes, 900 glioma tumors and 900 pituitary tumors. Each image was resized into 224 × 224 pixels, and then normalized by rescaling the pixels from [0, 255] to

TABLE 1. The summary of the layers of the Vgg19 model.

Layer	Type	Kernel Size	Output Shape
1	Input	-	224 × 224 × 3
2	Conv2D	3 × 3	224 × 224 × 64
3	Conv2D	3 × 3	224 × 224 × 64
4	Max-Pooling2D	2 × 2	112 × 112 × 64
5	Conv2D	3 × 3	112 × 112 × 128
6	Conv2D	3 × 3	112 × 112 × 128
7	Max-Pooling2D	2 × 2	56 × 56 × 128
8	Conv2D	3 × 3	56 × 56 × 256
9	Conv2D	3 × 3	56 × 56 × 256
10	Conv2D	3 × 3	56 × 56 × 256
11	Conv2D	3 × 3	56 × 56 × 256
12	Max-Pooling2D	2 × 2	28 × 28 × 256
13	Conv2D	3 × 3	28 × 28 × 512
14	Conv2D	3 × 3	28 × 28 × 512
15	Conv2D	3 × 3	28 × 28 × 512
16	Conv2D	3 × 3	28 × 28 × 512
17	Max-Pooling2D	2 × 2	14 × 14 × 512
18	Conv2D	3 × 3	14 × 14 × 1024
19	Conv2D	3 × 3	14 × 14 × 1024
20	Conv2D	3 × 3	14 × 14 × 1024
21	Conv2D	3 × 3	14 × 14 × 1024
22	Max-Pooling2D	2 × 2	7 × 7 × 1024
23	Fully Connected	-	4096
24	Fully Connected	-	4096
25	Fully Connected	-	1000
26	Output	-	2

Total trainable parameters: 2,325,568

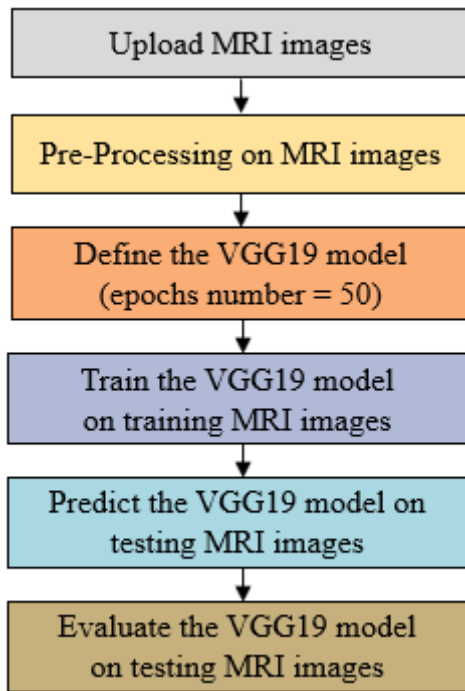[0, 1]. To minimize over-fitting, for VGG19, three data augmentation techniques were used to increase the original

FIGURE 3. The workflow of the VGG19.

FIGURE 4. Four samples of brain MRI images from the dataset used: (a) and (c) Glioma Tumors, (b) and (d) Pituitary Tumors.

dataset of glioma and pituitary images: rotation, width shift, and height shift. Each image was randomly rotated by 10°, with shifts in the width by up to 0.1, and shifts in the height by up to 0.1. Thus, the number of images in the dataset was increased by a factor of three.

Three data augmentation techniques were also used for the ResNext101_32 × 8d model: rotation, horizontal flip, and vertical flip. Each image was randomly rotated by 45°, with flips in the horizontal or vertical by up to 0.5.

The datasets were divided, the training sets were 75% for the VGG19 model and 85% for the ResNext101_32 × 8d model. Thus the corresponding test sets used to assess the two models were, respectively, 25% and 15% of the datasets.

D. EVALUATION METRICS
In this work, several well-known evaluation metrics were used to analyze model performance [45], [46]: Accuracy, Precision, Recall, F1-score, and the area under the receiver operating characteristic curve (ROCC). The ROCC is a means of comparing the accuracy of different classification models, to demonstrate the ability of a test to correctly identify those images with a tumor. The ROCC is a graph of the True Positive Rate (*TPR* - the images that were correctly diagnosed as having a tumor as a proportion of all images that did show a tumor) against the False Positive Rate (*FPR* – the images that were incorrectly diagnosed as having a tumor as a proportion of all images that did not show a tumor). The ranges for both TPR and FPR are between 0.0 and 0.1.

If *TP* = number of diseased samples correctly identified, *TN* = number of healthy samples correctly identified,
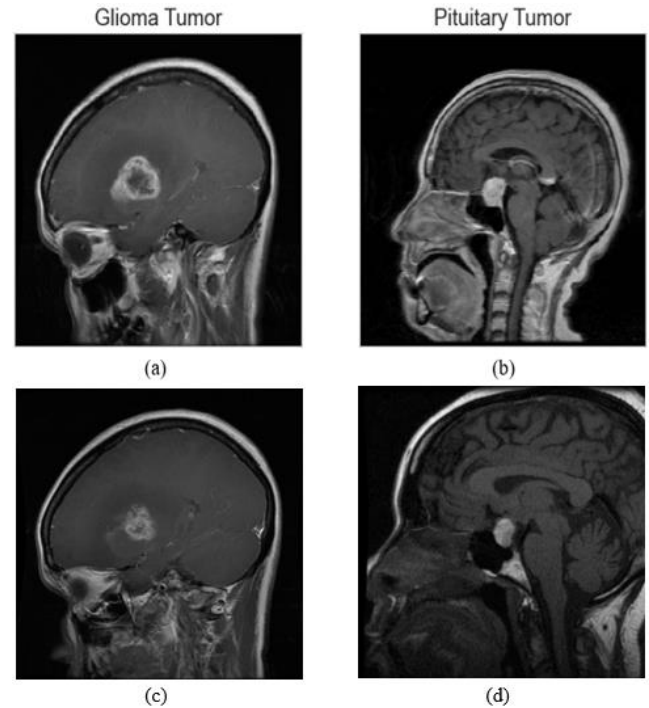
FN = the number of samples that were diseased but falsely diagnosed as healthy, and *FP* = the number of samples that were healthy and falsely diagnosed as diseased. Using these metrics, the total number of images in the dataset is *(TP + TN + FP + FN)*, and the total number correctly identified is *(TP + TN)*.

Accuracy of the model is the ratio of images accurately identified to the total number of images, see Eq. (2). Precision is the ratio of the number of images correctly diagnosed in a particular class, e.g., *TP*, to the total number of images diagnosed as in that class *(TP+FP)*, see Eq. (3). Recall or sensitivity, is the ratio of number of images correctly diagnosed *(TP)*, to the total number of correctly identified MRI images of both classes *(TP+FN)*, see Eq. (4). It is the probability of a positive test if the patient has a glioma tumor.

F1-score, or balanced F1-measure, is the harmonic mean of the Recall and Precision weighted by a factor of 2, see Eq. (5). The F1-score includes both *FN* and *FP,* so it can sometimes be a more useful metric than Accuracy.

AUC is the area under the ROCC, see Eq. (6). Note: $0 \leq$ AUC value ≤ 1 with higher values of AUC implying a model can successfully differentiate between different classes of MRI images. It follows that a model with a larger area under the ROCC, is more accurate than a model with a smaller area.

$$Accuracy = \frac{TP + TN}{TP + FP + TN + FN} \qquad (2)$$

$$Precision = \frac{TP}{TP + FP} \qquad (3)$$

$$Recall = \frac{TP}{TP + FN} \quad (4)$$

$$F1 - Measure = 2 \times \frac{Precision \times Recall}{Precision + Recall} \quad (5)$$

$$AUC = \int_0^1 TPRd(FPR) \quad (6)$$

In this work, the metrics used to evaluate the performance of the SISR technique based on the GAN algorithm are [47]: MSE (mean squared error), MS-SSIM (multiscale structural similarity index measure), PSNR (peak signal-to-noise ratio), and SSIM (structural similarity index measure) [48], [49], [50], [51], [52]. These metrics are calculated using Eqs. (7), (8), (9), and (10).

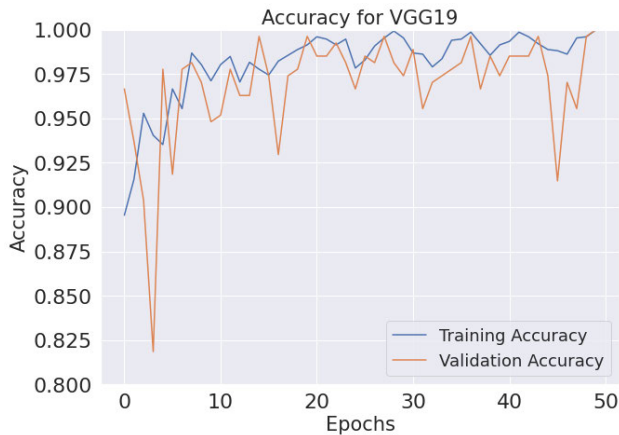$$MSE = \frac{1}{n} \sum_{k=1}^{n} \left(i_r(k) - i_y(k) \right)^2 \quad (7)$$

$$PSNR = 10 log_{10} \frac{MAX_i^2}{MSE} \quad (8)$$

$$SSIM = \frac{(2\mu_{ir}\mu_{iy} + c_1)(2 o_{iriy} + c_2)}{\left(\mu_{ir}^2 + \mu_{iy}^2 + c_1\right)\left(o_{ir}^2 + o_{iy}^2 + c_2\right)} \quad (9)$$

$$MS - SSIM = \frac{1}{nm} \sum_{p=0}^{n-1} \sum_{j=0}^{m-1} SSIM \quad (10)$$

V. EXPERIMENTAL RESULTS

Python in a Google Colab environment, with P100 GPU and 25 GB RAM memory was used to implement the proposed models.


FIGURE 5. Training and validation accuracy curves for VGG19.

Fig. 5 presents the training/learning and validation accuracies obtained for VGG19. The blue line symbolizes the training accuracy, which increases with increase in the number of epochs and approaches 100% after 50 epochs. The brown curve shows the validation accuracy, commencing at 97.56% and rising to 99.89% after 50 epochs. The training stopped at 50 epochs because the learning curve started to overfit. The number of training epochs was tuned for the highest training/ validation accuracy.
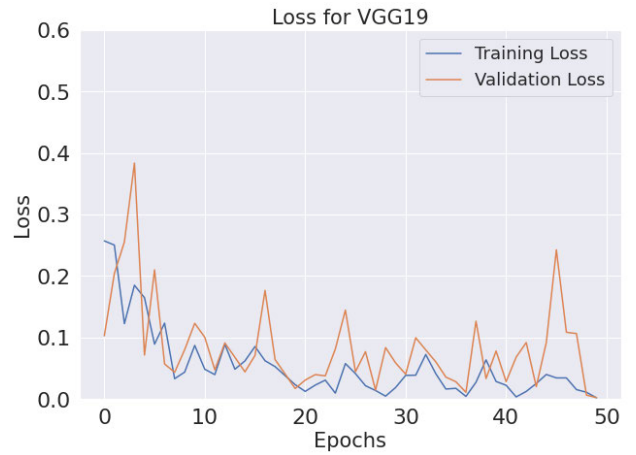
FIGURE 6. Training and validation loss curves for VGG19.

Fig. 6 shows the training/ validation loss curves for the VGG19 model, where the score of 0.0 would indicate perfect learning with no mistakes. Both losses continuously decreased as the number of epochs increased with the training loss reaching 0.0030 after 50 epochs, and validation loss commencing at 0.110 and declining to 0.0120.
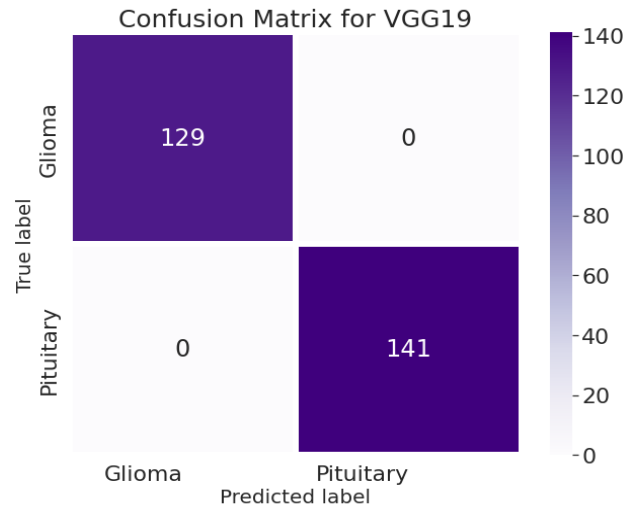
FIGURE 7. The error matrix for VGG19.

Figs. 7 and 8 present the error and normalized error matrices obtained from use of the VGG19. This matrix is used to evaluate model performance when classifying two classes, here using the MRI test dataset and comparing the predicted/true class outputs. The dark purple blocks on the matrix in Fig. 7 represent classification accuracy, while the values outside the blocks represent error values. Here, the error matrix shows, respectively, 129 and 141 true positives for the two classes of tumor, glioma, and pituitary. The normalized error matrix for VGG19 shows classification accuracy of 1.0 (100%) for glioma and pituitary classes, with zero classification error in both cases. The VGG19 model
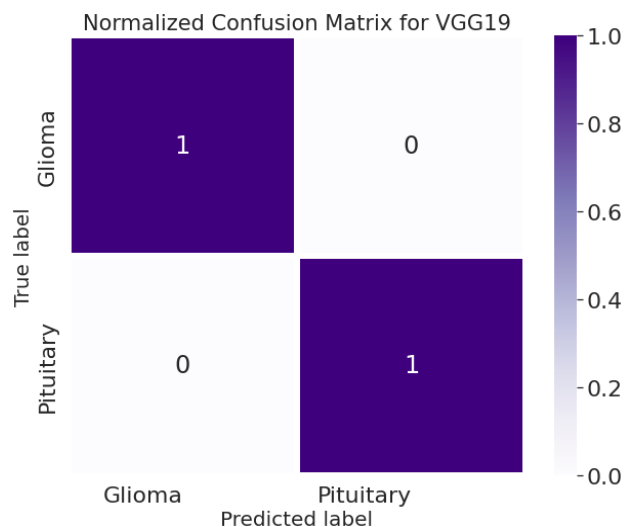
FIGURE 8. The normalized error matrix for VGG19.

FIGURE 9. Histograms of Glioma and Pituitary images.

performance contained no errors. The total number of glioma and pituitary tumors which taken for the testing error matrix is 270.

TABLE 2. Classification of precision, recall, and F1-score for the Vgg19 model.

Class	Precision	Recall	F1-score
Glioma	0.9907	0.9978	0.9992
Pituitary	0.9974	0.9900	0.9986
Accuracy	-	-	0.9989
Macro average	0.9990	0.9989	0.9989
Weighted average	0.9990	0.9989	0.9989

Table 2 presents the F1-score, Precision, and Recall for VGG19, by which to assess its performance for the dataset utilized. The values for F1-score, Precision, and Recall for the glioma and pituitary classes were, respectively, 99.92% and 99.86%, 99.07% and 99.74%, and 99.78% and 99.00%. The macro-average is determined by computing an evaluation metric independently for each class and then taking the mean. For the F1-score, Precision and Recall the respective macro-averages were: 99.89%, 99.90%, and 99.89%. We note, see Table 2, that the corresponding weighted averages had the same values.

Fig. 9 shows histograms for the glioma and pituitary images for VGG19. Precision-recall and ROCCs are presented in Figs. 10 and 11. Precision-recall curves present the precision rate as a function of the recall rate. Fig. 10 shows the precision-recall curves for VGG19 for both glioma and pituitary classes. The values of the areas under the precision-recall curves for both classes are 1.00 or 100%,
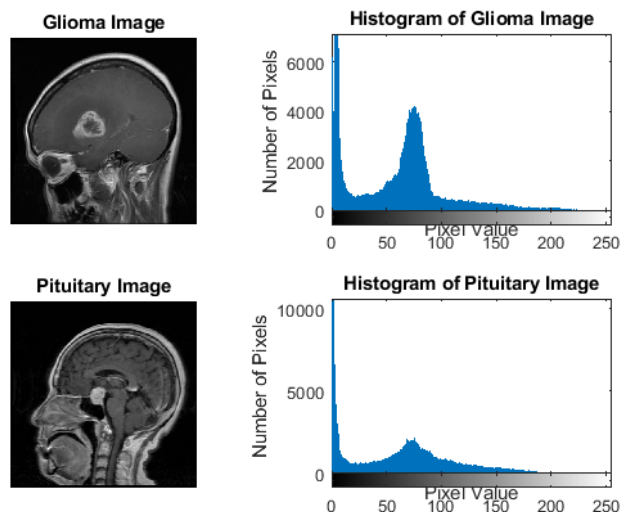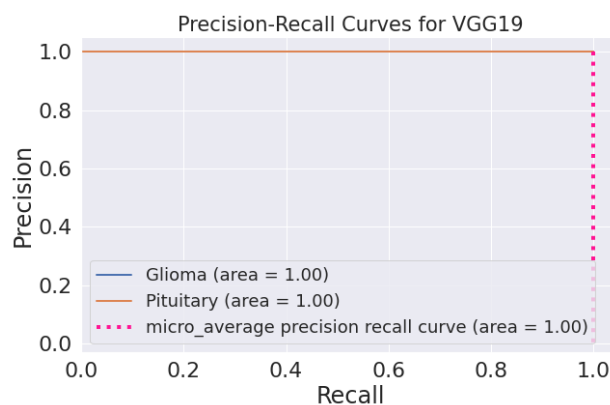

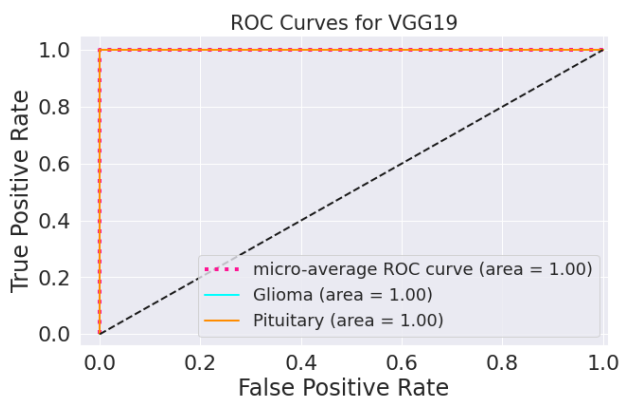**FIGURE 10.** Precision-recall curves for VGG19.

FIGURE 11. ROC curves for VGG19.

giving the corresponding values of the macro-average for both precision and recall of 1.00.

Fig. 11 shows the ROCC for VGG19, and it can be seen that the values of the areas for both classes are 1.00 or 100%, meaning the macro-average ROCC area is also 1.00. These results imply that VGG19 doesn't cause errors.

TABLE 3. Performance of the Vgg19 model for different *k*-fold cross-validations.

k-fold value	Accuracy (%)	Loss
1	98.66	0.0168
2	99.19	0.0125
3	99.58	0.0097
4	99.99	0.0291
5	99.33	0.0117
Average	**99.35**	**0.0113**

Table 3 presents performance data for the proposed VGG19 model using *k*-fold cross-validation, where *k* represents the number of equal partitions into which the data is divided. Here $k = 5$, one for validation and four for training. The model was trained five times using the different partitions, each time with an epoch number of 50. The average loss rate and accuracy rate for the model were 0.0113 and 99.35% respectively. Therefore, VGG19 achieved a high performance when using 5-cross-validation, avoiding bias in the results by using a suitable allocation of test and training datasets.
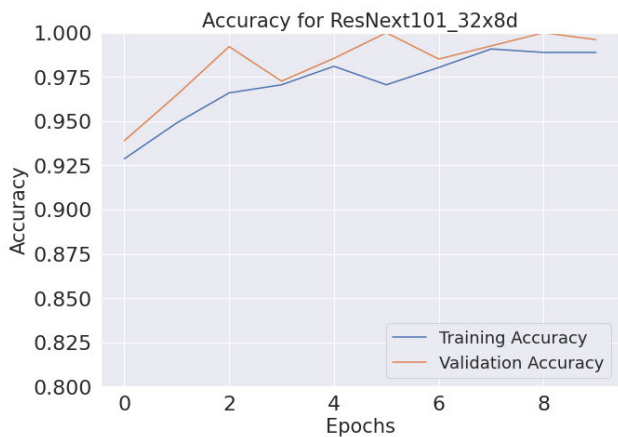
**FIGURE 12.** Training and validation accuracy curves for ResNext101_32 × 8d.

Training and validation accuracy for the ResNext101_32 × 8d model are shown in Fig. 12. The training accuracy increased with increase in number of epochs and achieved 98.88% after 10 epochs. The validation accuracy commenced at 93.75% and increased to 99.60% after 10 epochs.

Fig. 13 shows the loss rate curves for ResNext101_32 × 8d using the validation and training data sets. The numerical value of the loss rate diminished as the number of epochs

FIGURE 13. Training and validation loss curves for ResNext101_32 × 8d.

grew, after 10 epochs the value for the training data set had reached 0.0289 and 0.0121 for the validation data set.
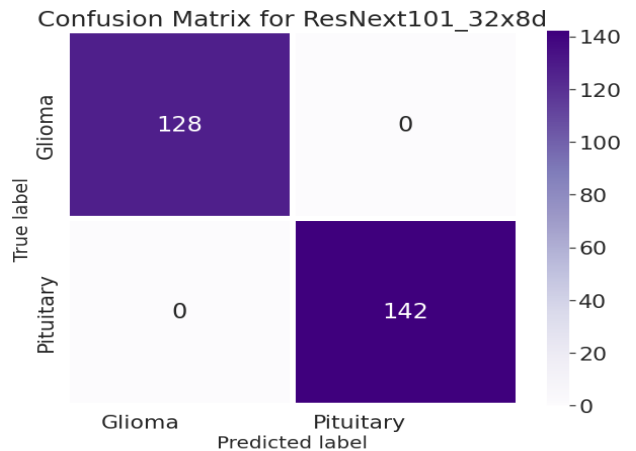
FIGURE 14. The error matrix for ResNext101_32 × 8d.

Fig. 14 shows the error matrix obtained using ResNext101_32 × 8d. The dark purple blocks show the classification accuracy. Here, the error matrix shows, respectively, 128 and 142 true positives for the two classes of tumor: glioma, and pituitary. The normalized error matrix for ResNext101_32 × 8d is illustrated in Fig. 15. It has a classification accuracy of 1.0 "100%" for glioma and pituitary classes, with zero classification errors.

Table 4 presents F1-score, Precision, and Recall metrics for ResNext101_32 × 8d, by which to assess its relative performance for the dataset used. For both the glioma and pituitary classes, the F1-score, Precision, and Recall were all 100%, as were the macro-averages and weighted averages.

Fig. 16 presents the precision-recall curves for ResNext101 _32 × 8d for both glioma and pituitary. The values of areas under the precision-recall curves for both classes are 1.00 or 100%. Therefore, the macro-average precision-recall curve area is 1.00. Fig. 17 shows the ROCCs for ResNext101_32 × 8d, and, again, the values of the areas under
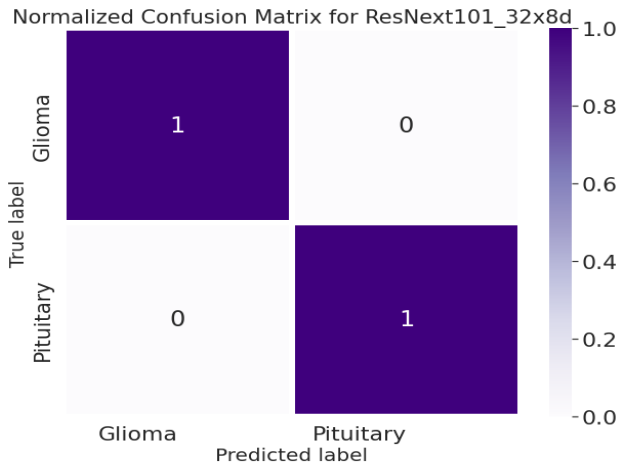
FIGURE 15. The normalized error matrix for ResNext101_32 × 8d.

TABLE 4. Classification of precision, recall, and F1-score for the proposed ResNext101_32 × 8d model.

Class	Precision	Recall	F1-score
Glioma	1.0000	1.0000	1.0000
Pituitary	1.0000	1.0000	1.0000
Accuracy	-	-	1.0000
Macro average	1.0000	1.0000	1.0000
Weighted average	1.0000	1.0000	1.0000
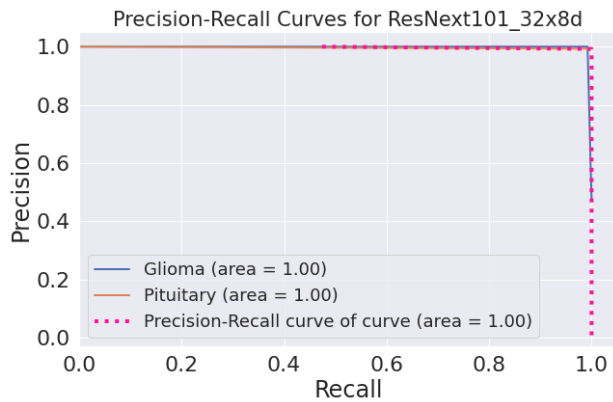
FIGURE 16. Precision-recall curves for ResNext101_32 × 8d.

FIGURE 17. ROC curves for ResNext101_32 × 8d.

TABLE 5. Comparison of the accuracy of proposed and previous models.

Reference	Model	Testing Accuracy (%)
[20, 2018]	CapsNet	86.56
[21, 2019]	CNN + GA	94.2
[22, 2019]	VGG-16	90
	Inception-V3	55
	ResNet-50	95
[23, 2019]	DenseNet-LSTM	92.13
[24, 2015]	SVM	91.28
[25, 2018]	CNN	84.19
[26, 2020]	KNN + nLBP	95.56
[27, 2018]	CNN + ELM	93.68
[28, 2009]	SVM-KNN	85
[29, 2019]	CapsNet	92.6
[30, 2019]	CNN	94.39
[31, 2020]	ANN	95.8
[32, 2020]	CNN	95.49
[33, 2020]	CNN	96
[34, 2021]	HMM	96.88
[35, 2021]	Xception	93.77
	Inception-V3	94.34
The Proposed Models	**VGG19**	**99.89**
	SISR + ResNext101_32x8d	**100**

the curves for both classes are 1.00 or 100%, indicating that ResNext101_32 × 8d doesn't generate errors.

Figs. 18, 19, and 20 show the results for the SISR technique. Fig. 18(a), Fig. 19(a) and Fig. 20(a) illustrate, respectivelt, a high-resolution, low-resolution and super-resolution imagese. Fig.s 18(b), 19(b), and 20(b) show the histograms for these images. It is clear that there are differences in the resolution of the images.

VI. DISCUSSION

The results presented above show that the ResNext101_32 × 8d and VGG19 models have a very high accuracy with low loss rate when trained and tested. Precision-recall curves, error matrices, and ROCCs demonstrated that the proposed models can accurately classify brain tumors.
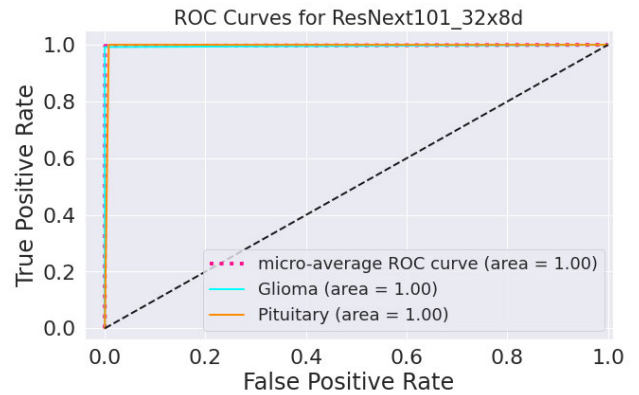
The performance of both models in terms of their training and validation accuracy curves are shown in Figs 5 and 12. Figs 6 and 13 show the model performance, in terms of loss rates, reached 0.0120 and 0.0108 for VGG19 and ResNext101_32 × 8d, respectively. Figs 7, 8, 14, and 15 present error rate distribution for the two classes and show that the models perform well. Figs 18, 19, and 20 show the image quality obtained using the SISR process.

Table 5 is a comparison of the accuracy achieved by the VGG19 and ResNext101_32 × 8d models with previously published results. We see that the testing accuracies of the proposed models are noticeably higher than those achieved by the models listed in references [20], [21], [22], [23], [24], [25], [26], [27], [28], [29], [30], [31], [32], [33], [34], and [35].
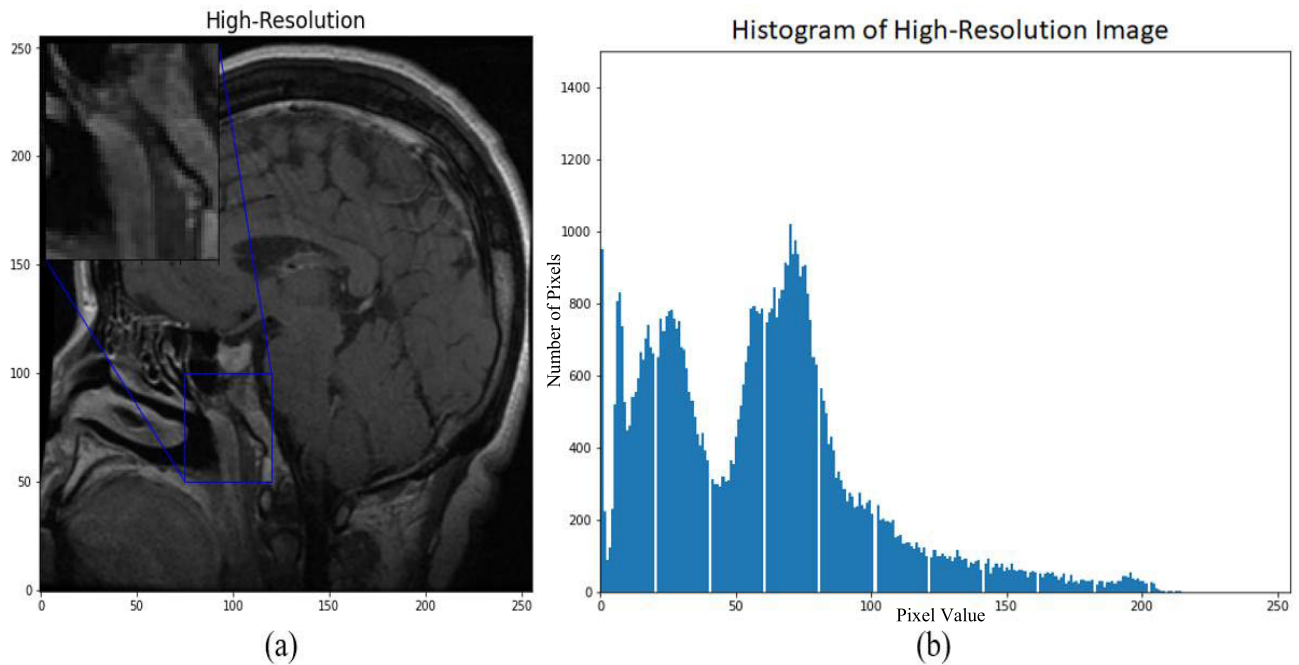
FIGURE 18. Results of high-resolution images: (a) High-Resolution MRI image, (b) Histogram of high-resolution image.
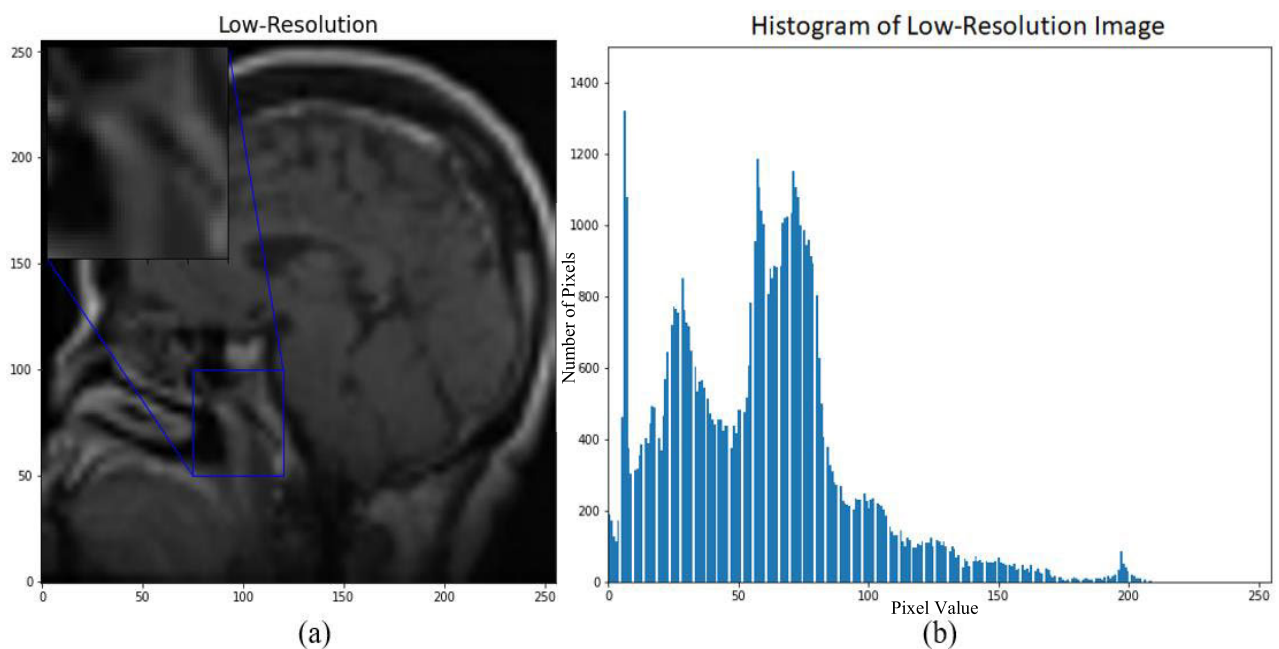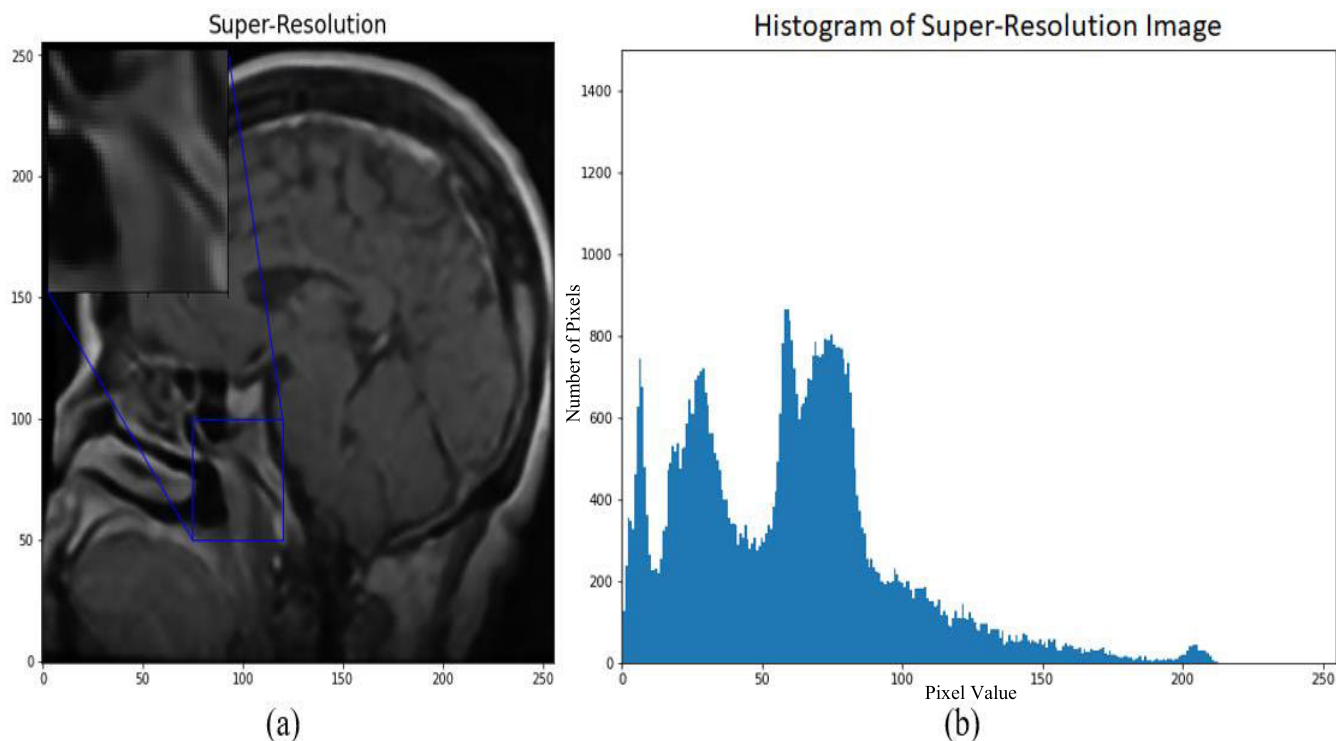

FIGURE 19. Results of low-resolution images: (a) Low-Resolution MRI image, (b) Histogram of low-resolution image.

The higher performance achieved is due to batch and kernel sizes, the fine-tuning of the models' hyper-parameters, loss activation functions, optimizer type, pool size, number of neurons utilized in the conv-layers, and number of training epochs.

For VGG19, setting the number of training epochs to 50, and batch size to 30, and using a softmax activation function with kernel and pool sizes of the convolutional and max-polling layers adjusted to 3×3 and 2×2 filters, respectively, VGG19 achieved a test accuracy of 99.89%.

However, when the batch size was changed to 64, the training epochs reconfigured to 40, with a sigmoid activation function, and kernel and pool sizes of the convolutional and max-polling layers set to 5×5 and 3×3 filters, respectively, the VGG19 testing accuracy reached only 95.78%. We conclude that the parametric settings can significantly enhance the results.

A GridSearchCV method was used to automatically compute the optimum values of the hyper-parameters to ensure the models achieved optimal performance.

FIGURE 20. Results of super-resolution images: (a) Super-Resolution MRI image, (b) Histogram of super-resolution image.

VII. CONCLUSION

This paper reports the application of ResNext101_32×8d and VGG19 DLMs to classify patients with glioma and pituitary tumors based on brain MRI images. The models were trained and assessed using a dataset of 900 each of glioma and pituitary images. In addition, a single image super-resolution (SISR) technique was applied to the MRI images to improve their resolution before classification using ResNext101_32 × 8d and VGG19. The SISR is based on a GAN algorithm and evaluated using MS-SSIM, PSNR, and SSIM metrics. The MS-SSIM was 96.39%, the PSNR was 29.30 dB, and the SSIM rate was 0.847. Experimental assessment of the accuracy of the VGG19 and ResNext101_32 × 8d models, showed the accuracy realized was 99.89% and 100% respectively, with respective test loss rates of 0.0120 and 0.0108.

The error matrix, F1-score, Precision, Recall, area under the precision-recall curve, and the ROCC have been presented and the models' performances evaluated. The VGG19 model's F1-score was 99.89%, its precision score was 99.90%, and the achieved recall was 99.89%. The corresponding precision-recall curves for the VGG19, for both glioma and pituitary tumors was 100%. The area under the ROCC is 100% for both classes for the VGG19.

The ResNext101_32 × 8d model's F1-score, precision, and recall were all 100%. The achieved areas under the ROC and precision-recall curves were 100% for both classes glioma tumor and pituitary tumor. Models such as these assist specialist doctors by providing a fast identification of patients with brain tumors, which makes these models useful tools for rapid screening and providing support for medical diagnoses.

The hyper-parameters of both ResNext101_32 × 8d and VGG19 i.e., batch and kernel sizes, fine-tuning the models' hyper-parameters, loss activation functions, optimizer type, pool size, number of neurons used in the conv-layers and number of training epochs. were found to substantially impact the accuracy of the results. Best performance depends on achieving the optimal settings for these parameters.

The obtained results demonstrate that the pre-trained ResNext101_32 × 8d and VGG19 models achieved high performance when classifying brain tumors. To assess the performance of VGG19 in terms of testing accuracy and loss 5-fold cross-validation was used. Both the ResNext101_32 × 8d and VGG19 models can be applied to MRI medical images to speed up diagnosis for the benefit of both patients and doctors.

Future work should include applying the models proposed here to more brain MRI images, possibly also adding other pre-trained DLMs, such as ResNet-18 and AlexNet, to the utilized dataset.

REFERENCES

[1] H. H. Sultan, N. M. Salem, and W. Al-Atabany, "Multi-classification of brain tumor images using deep neural network," *IEEE Access*, vol. 7, pp. 69215–69225, 2019.

[2] M. B. Naceur, M. Akil, R. Saouli, and R. Kachouri, "Fully automatic brain tumor segmentation with deep learning-based selective attention using overlapping patches and multi-class weighted cross-entropy," *Med. Image Anal.*, vol. 63, Jul. 2020, Art. no. 101692.

[3] J. Paul and T. S. Sivarani, "RETRACTED ARTICLE: Computer aided diagnosis of brain tumor using novel classification techniques," *J. Ambient Intell. Humanized Comput.*, vol. 12, no. 7, pp. 7499–7509, Jul. 2021.

[4] S. Bauer, R. Wiest, L.-P. Nolte, and M. Reyes, "A survey of MRI-based medical image analysis for brain tumor studies," *Phys. Med. Biol.*, vol. 58, no. 13, pp. R97–R129, Jul. 2013.

[5] M. Pantoja, M. Weyrich, and G. Fernández-Escribano, "Acceleration of MRI analysis using multicore and manycore paradigms," *J. Supercomput.*, vol. 76, no. 11, pp. 8679–8690, Nov. 2020.

[6] Q. T. Ostrom, H. Gittleman, G. Truitt, A. Boscia, C. Kruchko, and J. S. Barnholtz-Sloan, "CBTRUS statistical report: Primary brain and other central nervous system tumors diagnosed in the United States in 2014–2018," *Neuro Oncol*, vol. 23, no. 12, pp. iii1–iii105, 2021.

[7] S. Bakas et al., "Identifying the best machine learning algorithms for brain tumor segmentation progression assessment and overall survival prediction in the BRATS challenge," 2018, *arXiv:1811.02629*.

[8] L. Zhang and H. Schaeffer, "Forward stability of ResNet and its variants," *J. Math. Imag. Vis.*, vol. 62, no. 3, pp. 328–351, Apr. 2020.

[9] K. Simonyan and A. Zisserman, "Very deep convolutional networks for large-scale image recognition," in *Proc. 3rd Int. Conf. Learn. Represent.*, San Diego, CA, USA, May 2015.

[10] G. Huang, Z. Liu, L. Van Der Maaten, and K. Q. Weinberger, "Densely connected convolutional networks," in *Proc. IEEE Conf. Comput. Vis. Pattern Recognit. (CVPR)*, Jul. 2017, pp. 2261–2269.

[11] K. He, X. Zhang, S. Ren, and J. Sun, "Deep residual learning for image recognition," in *Proc. IEEE Conf. Comput. Vis. Pattern Recognit. (CVPR)*, Jun. 2016, pp. 770–778.

[12] P. Aswathy, Siddhartha, and D. Mishra, "Deep GoogLeNet features for visual object tracking," in *Proc. IEEE 13th Int. Conf. Ind. Inf. Syst. (ICIIS)*, Dec. 2018, pp. 60–66.

[13] A. Krizhevsky, I. Sutskever, and G. E. Hinton, "ImageNet classification with deep convolutional neural networks," *Commun. ACM*, vol. 60, no. 6, pp. 84–90, May 2017.

[14] J. Deng, W. Dong, R. Socher, L.-J. Li, K. Li, and L. Fei-Fei, "ImageNet: A large-scale image database," in *Proc. IEEE Conf. Comput. Vis. Pattern Recognit.*, Jun. 2009, pp. 248–255.

[15] M. Tan and Q. Le, "EfficientNet: Rethinking model scaling for convolutional neural networks," in *Proc. 36th Int. Conf. Mach. Learn., Mach. Learn. Res.*, 2019, pp. 6105–6114. [Online]. Available: http://proceedings.mlr.press/v97/tan19a.html

[16] D. Yu and L. Deng, *Automatic Speech Recognition*. Cham, Switzerland: Springer, 2016.

[17] P. Klosowski, "Deep learning for natural language processing and language modelling," in *Proc. Signal Process., Algorithms, Archit., Arrangements, Appl. (SPA)*, Sep. 2018, pp. 223–228.

[18] S. Mohsen, A. Elkaseer, and S. G. Scholz, "Industry 4.0-oriented deep learning models for human activity recognition," *IEEE Access*, vol. 9, pp. 150508–150521, 2021.

[19] C. Szegedy, W. Liu, Y. Jia, P. Sermanet, S. Reed, D. Anguelov, D. Erhan, V. Vanhoucke, and A. Rabinovich, "Going deeper with convolutions," in *Proc. IEEE Conf. Comput. Vis. Pattern Recognit. (CVPR)*, Jun. 2015, pp. 1–9.

[20] P. Afshar, A. Mohammadi, and K. N. Plataniotis, "Brain tumor type classification via capsule networks," in *Proc. 25th IEEE Int. Conf. Image Process. (ICIP)*, Oct. 2018, pp. 3129–3133.

[21] A. K. Anaraki, M. Ayati, and F. Kazemi, "Magnetic resonance imaging-based brain tumor grades classification and grading via convolutional neural networks and genetic algorithms," *Biocybern. Biomed. Eng.*, vol. 39, no. 1, pp. 63–74, Jan. 2019.

[22] P. Saxena, A. Maheshwari, and S. Maheshwari, "Predictive modeling of brain tumor: A deep learning approach," in *Innovations in Computational Intelligence and Computer Vision*, vol. 1189, M. K. Sharma, V. S. Dhaka, T. Perumal, N. Dey, and J. M. R. S. Tavares, Eds. Singapore: Springer, 2021, pp. 275–285.

[23] Y. Zhou, Z. Li, H. Zhu, C. Chen, M. Gao, K. Xu, and J. Xu, "Holistic brain tumor screening and classifcation based on DenseNet and recurrent neural network," in *Brainlesion: Glioma, Multiple Sclerosis, Stroke and Traumatic Brain Injuries*. Cham, Switzerland: Springer, 2019, pp. 208–217.

[24] J. Cheng, W. Huang, S. Cao, R. Yang, W. Yang, Z. Yun, Z. Wang, and Q. Feng, "Correction: Enhanced performance of brain tumor classification via tumor region augmentation and partition," *PLoS ONE*, vol. 10, no. 12, Dec. 2015, Art. no. e0144479.

[25] N. Abiwinanda, M. Hanif, S. Hesaputra, A. Handayani, and T. Mengko, "Brain tumor classifcation using convolutional neural network," in *World Congress on Medical Physics and Biomedical Engineering 2018*. Singapore: Springer, 2018, pp. 183–189.

[26] K. Kaplan, Y. Kaya, M. Kuncan, and H. M. Ertunç, "Brain tumor classification using modified local binary patterns (LBP) feature extraction methods," *Med. Hypotheses*, vol. 139, Jun. 2020, Art. no. 109696.

[27] A. Pashaei, H. Sajedi, and N. Jazayeri, "Brain tumor classification via convolutional neural network and extreme learning machines," in *Proc. 8th Int. Conf. Comput. Knowl. Eng. (ICCKE)*, Oct. 2018, pp. 314–319.

[28] E. I. Zacharaki, S. Wang, S. Chawla, D. Soo Yoo, R. Wolf, E. R. Melhem, and C. Davatzikos, "Classification of brain tumor type and grade using MRI texture and shape in a machine learning scheme," *Magn. Reson. Med.*, vol. 62, no. 6, pp. 1609–1618, Dec. 2009.

[29] R. V. Kurup, V. Sowmya, and K. P. Soman, "Effect of data pre-processing on brain tumor classifcation using capsulenet," in *Proc. Int. Conf. Intell. Comput. Commun. Technol.*, Berlin, Germany: Springer, 2019, pp. 110–119.

[30] S. Das, O. F. M. R. R. Aranya, and N. N. Labiba, "Brain tumor classification using convolutional neural network," in *Proc. 1st Int. Conf. Adv. Sci., Eng. Robot. Technol. (ICASERT)*, 2019, pp. 1–5.

[31] Z. Ullah, M. U. Farooq, S.-H. Lee, and D. An, "A hybrid image enhancement based brain MRI images classification technique," *Med. Hypotheses*, vol. 143, Oct. 2020, Art. no. 109922.

[32] Z. Huang, X. Du, L. Chen, Y. Li, M. Liu, Y. Chou, and L. Jin, "Convolutional neural network based on complex networks for brain tumor image classification with a modified activation function," *IEEE Access*, vol. 8, pp. 89281–89290, 2020.

[33] T. Kalaiselvi, S. T. Padmapriya, P. Sriramakrishnan, and K. Somasundaram, "Deriving tumor detection models using convolutional neural networks from MRI of human brain scans," *Int. J. Inf. Technol.*, vol. 12, no. 2, pp. 403–408, Jun. 2020.

[34] G. Li, J. Sun, Y. Song, J. Qu, Z. Zhu, and M. R. Khosravi, "Real-time classification of brain tumors in MRI images with a convolutional operator-based hidden Markov model," *J. Real-Time Image Process.*, vol. 18, no. 4, pp. 1207–1219, Aug. 2021.

[35] N. Noreen, S. Palaniappan, A. Qayyum, I. Ahmad, and M. O. Alassafi, "Brain tumor classification based on fine-tuned models and the ensemble method," *Comput., Mater. Continua*, vol. 67, no. 3, pp. 3967–3982, 2021.

[36] A. Rehman, M. A. Khan, T. Saba, Z. Mehmood, U. Tariq, and N. Ayesha, "Microscopic brain tumor detection and classification using 3D CNN and feature selection architecture," *Microsc. Res. Technique*, vol. 84, no. 1, pp. 133–149, Jan. 2021.

[37] A. Rehman, S. Naz, M. I. Razzak, F. Akram, and M. Imran, "A deep learning-based framework for automatic brain tumors classification using transfer learning," *Circuits, Syst., Signal Process.*, vol. 39, no. 2, pp. 757–775, Feb. 2020.

[38] M. I. Sharif, J. P. Li, M. A. Khan, and M. A. Saleem, "Active deep neural network features selection for segmentation and recognition of brain tumors using MRI images," *Pattern Recognit. Lett.*, vol. 129, pp. 181–189, Jan. 2020.

[39] S. R. Muzammil, S. Maqsood, S. Haider, and R. Damaševičius, "CSID: A novel multimodal image fusion algorithm for enhanced clinical diagnosis," *Diagnostics*, vol. 10, no. 11, p. 904, Nov. 2020.

[40] S. Maqsood, R. Damasevicius, and F. M. Shah, "An efficient approach for the detection of brain tumor using fuzzy logic and U-NET CNN classification," in *Proc. Int. Conf. Comput. Sci. Appl.*, vol. 12953. Cham, Switzerland: Springer, 2021, pp. 105–118.

[41] H. Samma, S. A. Suandi, N. A. Ismail, S. Sulaiman, and L. L. Ping, "Evolving pre-trained CNN using two-layers optimizer for road damage detection from drone images," *IEEE Access*, vol. 9, pp. 158215–158226, 2021.

[42] J. A. Gamble and J. Huang, "Convolutional neural network for human activity recognition and identification," in *Proc. IEEE Int. Syst. Conf. (SysCon)*, Aug. 2020, pp. 1–7.

[43] D. P. Kingma and J. Ba, "Adam: A method for stochastic optimization," 2014, *arXiv:1412.6980*.

[44] (2021). *Brain-Tumor-Datasets*. Kaggle Repository. Accessed: Dec. 2021. [Online]. Available: https://www.kaggle.com/drsaeedmohsen/braintumordatasets

[45] R. Vinayakumar, M. Alazab, K. P. Soman, P. Poornachandran, A. Al-Nemrat, and S. Venkatraman, "Deep learning approach for intelligent intrusion detection system," *IEEE Access*, vol. 7, pp. 41525–41550, 2019.

[46] S. Mohsen, A. Elkaseer, and S. G. Scholz, "Human activity recognition using k-nearest neighbor machine learning algorithm," *Proc. 8th Int. Conf. Sustain. Design Manuf. (KES-SDM)*, 2021, pp. 304–313.

[47] W. El-Shafai, E. M. Mohamed, M. Zeghid, A. M. Ali, and M. H. Aly, "Hybrid single image super-resolution algorithm for medical images," *Comput., Mater. Continua*, vol. 72, no. 3, pp. 4879–4896, 2022.

[48] Z. Wang, A. C. Bovik, H. R. Sheikh, and E. P. Simoncelli, "Image quality assessment: From error visibility to structural similarity," *IEEE Trans. Image Process.*, vol. 13, no. 4, pp. 600–612, Apr. 2004.

[49] W. Lin and C.-C. J. Kuo, "Perceptual visual quality metrics: A survey," *J. Vis. Commun. Image Represent.*, vol. 22, no. 4, pp. 297–312, May 2011.

[50] Z. Wang, E. Simoncelli, and A. Bovik, "Multiscale structural similarity for image quality assessment," *Signals, Syst. Comput.*, vol. 2, no. 3, pp. 1398–1402, 2003.

[51] W. El-Shafai, S. A. El-Nabi, E.-S. M. El-Rabaie, A. M. Ali, N. F. Soliman, A. D. Algarni, and F. E. Abd El-Samie, "Efficient deep-learning-based autoencoder denoising approach for medical image diagnosis," *Comput., Mater. Continua*, vol. 70, no. 3, pp. 6107–6125, 2022.

[52] W. El-Shafai, A. A. Mahmoud, A. M. Ali, E.-S. M. El-Rabaie, T. E. Taha, O. F. Zahran, A. S. El-Fishawy, N. F. Soliman, A. A. Alhussan, and F. E. Abd El-Samie, "Deep CNN model for multimodal medical image denoising," *Comput., Mater. Continua*, vol. 73, no. 2, pp. 3795–3814, 2022.

SAEED MOHSEN received the B.Sc. degree (Hons.) in electronics engineering and electrical communications from the Thebes Higher Institute, Cairo, Egypt, in 2013, and the M.Sc. and Ph.D. degrees in electrical engineering from Ain Shams University, Cairo, in 2016 and 2020, respectively. He is currently an Assistant Professor with the Al-Madinah Higher Institute for Engineering and Technology, Giza, Egypt. He made intensive research on applications of artificial intelligence (AI), such as deep learning and machine learning. He has published a number of papers in specialized international conferences and peer-reviewed periodicals. His current research interests include biomedical engineering, wearable devices, energy harvesting, analog electronics, and the Internet of Things (IoT).

ANAS M. ALI was born in Alexandria, Egypt. He received the B.Sc. degree (Hons.) in electronics and communication engineering from the Alexandria Higher Institute of Engineering and Technology (AIET), Alexandria, Egypt, in 2016, and the M.Sc. degree in communications and electronics engineering from Menoufia University, in 2021. He is currently a Researcher Assistant with the Robotics and Internet-of-Things Laboratory, Prince Sultan University, Riyadh, Saudi Arabia. His research interests include image and video signal processing, medical image processing, the Internet of Things, medical diagnoses applications, image and video magnification, artificial intelligence for signal processing algorithms, deep learning in signal processing, modulation identification and classification, and image restoration.

EL-SAYED M. EL-RABAIE received the B.Sc. degree (Hons.) in radio communications from Tanta University, Tanta, Egypt, in 1976, the M.Sc. degree in communication systems from Menoufia University, Menouf, Egypt, in 1981, and the Ph.D. degree in microwave device engineering from the Queen's University of Belfast, Belfast, U.K., in 1986. In his doctoral research, he has constructed a computer-aided design (CAD) package used in nonlinear circuit simulations-based on the harmonic balance techniques. Until February 1989, he was a Postdoctoral Fellow with the Department of Electronic Engineering, Queen's University of Belfast. He was invited as a Research Fellow with the College of Engineering and Technology, Northern Arizona University, Flagstaff, in 1992; and a Visiting Professor with Ecole Polytechnique de Montréal, Montreal, QC, Canada, in 1994. He is a Reviewer of Quality Assurance and Accreditation of Egyptian Higher Education and a member of the Scientific Committee for the promotion of professors and assistant professors, from 2019 to 2022. He has authored or coauthored more than 500 papers and 21 text books. His current research interests include device characterization, digital communication systems, and digital image processing. He acts as a reviewer and a member of the editorial board of several scientific journals.

AHMED ELKASEER received the Ph.D. degree from the Cardiff School of Engineering, Cardiff University, U.K., in 2011. He is a Senior Research Fellow with the Institute for Automation and Applied Informatics (IAI), Karlsruhe Institute of Technology (KIT), Germany. He has more than 20 years of research experience in advanced manufacturing technologies. He has been working on different EC and EPSRC funded research projects. His work entails performing experimental and laboratory work, modeling, simulation, and optimization-based studies of mechanical, EDM, and laser processing of advanced materials on conventional and micro scales, with a recent emphasis on additive and smart manufacturing and Industry 4.0 applications. His studies have led to several publications in the area of conventional and advanced micro-and nano-manufacturing technologies. He serves as a guest editor, an associate editor, an editorial board member, and a reviewer for a number of journals. He was a scientific committee chair and a program committee member of a number of international conferences.

STEFFEN G. SCHOLZ is the Head of the Process Optimization, Information Management and Applications Research Team, Institute for Automation and Applied Informatics (IAI), Karlsruhe Institute of Technology. He is also an Honorary Professor with Swansea University, U.K., and an Adjunct Professor with the Vellore Institute of Technology, India. He is also the Principal Investigator in the Helmholtz funded long-term programs, such as Digital System Integration and Printed Materials and Systems. He has more than 22 years of experience in the field of system integration and automation, sustainable flexible production, polymer micro- and nano-replication, process optimization and control, with a recent emphasis on additive manufacturing and Industry 4.0 applications. In addition to pursuing and leading research, he is very active with knowledge transfer to industry. He has involved in over 30 national and international projects. He has won in excess of 20M EUR research grants, in which he has acted as a coordinator and/or a principal investigator. His academic output includes more than 150 technical papers and five books. He is the chair of different international conferences with the scope of advanced and sustainable manufacturing technologies.

ASHRAF MOHAMED ALI HASSAN was born in Giza, in 1979. He received the B.Sc. (Hons.), M.Sc., and Ph.D. degrees in electrical engineering from Cairo University, in 2002, 2005, and 2009, respectively. He is an Associate Professor with the October High Institute for Engineering and Technology, 6th of October, Egypt. He has published more than 25 international papers. He received a certificate of appreciation for the supervision with the high performance and lasting contribution to the graduation project titled "Vertical Handover Implementation and Application" which is the first on the level of the Egyptian university. His research interests include digital signal processing and synthesis of electronic circuits. He has awarded an Associate Professor of electronics and communication engineering from Supreme Council of Universities, Egypt, in 2019.